

Item DR1. Petrophysical Properties of Undeformed and Faulted Sediments

We measured the grain size distribution of natural undeformed and faulted sediments from the three studied fault zones (n=32 samples), *in situ* air-permeability across a selected fault zone (Fault 1, see Fig. 3b), porosity and pore size distribution of representative undeformed and faulted samples (n=6 samples). Grain size and pore size distribution curves, and related statistical parameters, are shown below.

Grain Size distributions

To obtain particle size distributions of both undeformed and faulted sediments, we used a well established analytical procedure (e.g., Storti and Balsamo, 2010) that includes systematic preliminary tests preceding data acquisition. Further details are provided in the online Data Repository DR1. We used a Mastersizer 2000 laser diffraction particle size analyzer manufactured by Malvern Instruments (UK) equipped with a Hydro MU wet dispersion unit and analytical size range of 0.2–2000 μm . Before measurements, all samples were sieved at 1700 μm to account for shape anisotropy of coarser particles. Representative sub-samples (1-3 g) were obtained by a Quantachrome sieving riffler and rotary sample splitter. After preliminary tests (Balsamo and Storti, 2011), analyses were performed using the Hydro MU wet dispersion unit, decalcified water as dispersant liquid (refraction index 1.33), and 1.544 and 0.01 as refraction index and adsorbent coefficient of quartz grains, respectively. Pump speed velocity was fixed at 1900 revolution per minute; the measure run time at 10 s; no ultrasonication was used.

Statistical parameters of analysed samples from the three fault zones are reported in Table 1 DR1. The span values in Table 1 DR1 represent the measurement of the width of the distribution (i.e. the sorting degree) computed by the Malvern Mastersizer 2000 software as (percentile 0.9 – percentile 0.1) / (percentile 0.5). Narrower distributions mean better sorting, and smaller span values.

Grain size distribution curves of all analyzed samples are shown in Figures 1 DR1 (Fault 1) and 2 DR1 (Fault 2 and 3). Undeformed samples are in blue shade, whereas single deformation bands, zone of deformation bands and shear bands in damage zone are in green shade; foliated cataclasites within the fault core are in orange shade, and black gouges are in red. Each grain size distribution curve is obtained by averaging 25 measurements on the same sample.

Undeformed samples consist of well sorted, fine- to coarse-grained sands with unimodal distributions and clay-size content < 3 % (Figures 1 and 2 DR1). Single deformation bands, zone of deformation bands and shear bands in damage zone domain, as well as foliated cataclasites in fault core, have invariably lower mean grain size with respect to the undeformed counterparts, are moderately to poorly sorted as indicated by higher grain size span values, and have clay size fraction generally < 10%, with the exception of sample RN 9.5 (Fault 1). Different curves of deformed samples reflect different amount of grain comminution, which in turn most likely depend on the amount of displacement. Black gouges (red curves) have very similar grain size distributions

and consist of very fine-grained, very poorly sorted granular material with clay-size fraction up to 20 %.

Microstructural characterization

For microstructural analysis, blue epoxy-impregnated natural and experimental products were analyzed under a standard petrographic microscope and under a Philips XL30 scanning electronic microscope (SEM). Thin sections were oriented parallel to the slickenlines and orthogonal to the fault zone foliation. Grain angularity ($A = \text{Perimeter}^2/\text{Area}$) of experimentally sheared sands was calculated in 4 selected SEM images by image analysis technique with Optimas® software (e.g., Storti et al., 2007).

In-situ air-permeability

In-situ permeability measurements were performed by a TinyPerm II portable air permeameter manufactured by New England Research. This has a 5 mm nozzle and provides reliable permeability values from 10^9 – 10^{15} m² range (e.g., Balsamo et al., 2013 and reference therein). Data in different structural domains were acquired by multiple spot measurements in vertical sections.

Porosity and pore size distributions

A PoreMaster 33 system (Quantchrome Instruments) is used to measure porosity and pore size distribution by mercury-injection porosimetry. A total of 5 samples from the three fault zones were analyzed: one undeformed sand, two foliated cataclasites, and two black gouges. Before measurement, samples were dried at 40°C for 24 h, and then ~1.5-2 g of sub-sample were analyzed. Parameters used for measurements are as follows: sample cell is 1.0 × 3.0 cm, pressure range is 0.5 - 33000 psi, pore size range is 0.0064 to 950 μm, contact angle of mercury is 140 degrees, and surface tension of mercury is 0.48 N/m (480 dyn/cm). In mercury porosimetry analysis, the volume of mercury penetrating into porous samples can be measured as a function of the applied hydraulic pressure. The obtained mercury intrusion and extrusion curves were interpreted into pore size distributions in terms of the Washburn equation, in which the applied hydraulic pressure P is related to the cross-sectional radius R of pore-throats accessible by the pressured mercury, together with two material-related thermodynamic parameters: surface tension of mercury γ and its contact angle θ with the sample material involved (Washburn, 1921; Leon y Leon, 1998):

$$R = \frac{2\gamma \cdot \cos \theta}{P}$$

Pore size distributions of analysed samples are shown in Figure 3 DR1. We preliminary measured the sample RN29A two times to confirm that the reproducibility of the measurements was consistent with the experimental uncertainties (compare diagrams and statistical values of Fig. 3d-e DR1). Interparticle porosity of undeformed sand is 25.9 %, with unimodal pore size distribution and mean pore diameter of 24 μm (Fig. 3a DR1). Foliated cataclasites have porosity of 4.5 and 0.13 %, with both unimodal and polimodal distributions, and mean pore size of 0.34 and 0.32 μm, respectively (Fig. 3b-c DR1). Black gouges have total interparticle porosity between 0.17 and 0.91 %, unimodal distributions and the smaller mean pore sizes of 0.05 and 0.016 mm (Fig. 3d-f DR1).

Item DR2. Mineralogical Composition of Undeformed and Faulted Sediments

X-Ray diffraction (XRD) analyses on undeformed and faulted sediments and experimental products were performed using a Scintag X1 system (CuK α radiation) at 40 kV and 45 mA. Analytical details and results are shown in the online Data Repository DR2.

Natural samples

We report the X-ray diffraction (XRD) semi-quantitative analyses of bulk (Tab. 2 DR2) and clay-size fractions (<2 μm equivalent spherical diameter, Tab. 3 DR2) of undeformed and faulted sediments. Randomly oriented whole-rock powders were run in the 2–70 $^{\circ}2\theta$ interval with a step size of 0.05 $^{\circ}2\theta$ and a counting time of 3 s per step (Fig. 4a-c DR2). Oriented air-dried and ethylene-glycol-solvated samples of the <2 mm grain size fractions were scanned from 1 to 48 $^{\circ}2\theta$ and from 1 to 30 $^{\circ}2\theta$, respectively, with a step size of 0.05 $^{\circ}2\theta$ and a count time of 4 s per step (Fig. 4d-f DR2).

Peaks in relatively close position were selected for clay mineral quantitative analysis of the <2 μm fraction in order to minimize the angle-dependent intensity effect. Non-clay minerals that were observed in the <2 μm fraction were not included in the semi-quantitative analysis of the oriented aggregates, thus data only refer to the phyllosilicate group. Composite peaks were decomposed using Pearson VII functions and the DMSNT Scintag associated program. The illite and chlorite content in mixed-layer I-S and C-S was determined according to Moore and Reynolds (1997) using the delta two-theta method after decomposing the composite peaks between 9–10 $^{\circ}2\theta$ and 16–17 $^{\circ}2\theta$ for I-S and between 10–12.3 $^{\circ}2\theta$ and 25–26 $^{\circ}2\theta$ for C-S. The I-S stacking order (Reichweite parameter, R) was determined by the position of the I 001–S 001 reflection between 5 and 8.5 $^{\circ}2\theta$.

Both undeformed and faulted sediments consists of quartz, plagioclase, K-feldspar, phyllosilicates (clay minerals, chlorite and mica), calcite and small amounts of ankerite (Fig.4 A-C DR2). Among major minerals, quartz content ranges from 27 to 41%, albite from 16 to 38% and phyllosilicates from 13 to 24 (49% in sample RN9g, Tab. 2 DR2). K-feldspar and calcite have a weight percent <10% with average content of 7% and 5% respectively. Occasionally dolomite occurs in the black gouge.

In the clay mineral fraction, mineral abundance and composition changes amongst structural domains of faults. Host sediments show an illite rich-composition (56% mean value) with subordinate amounts of kaolinite (18%), chlorite (17%) and random ordered (R0) mixed layers I-S (Tab. 2 DR2; Fig. 4d DR2). Samples from the damage zone and foliated cataclasites in the fault core, do not show significant variations of clay mineral assemblages with respect to the protolith in terms of mineral abundance and mixed layer I-S composition. Only sample RN9g, located in the fault core next to the black gouge layer, display R1 mixed layers I-S and the neoformation of palygorskite (24%) and mixed layers chlorite-smectite (19%) (Fig. 4b and e DR2). Black gouges show the peculiar formation of authigenic pyrophyllite (<4%) and long-ordered R3 mixed layers I-S (Fig. 4c and f DR2).

Experimentally sheared gouges

Undeformed sediments were sheared at seismic slip rate of 1 m/s and normal stress of 14 MPa and then analysed by XRD (CuK α radiation) at 40 kV and 45 mA. Randomly oriented whole-rock powders were run in the 2–70 °2 θ interval with a step size of 0.05 °2 θ and a counting time of 3 s per step (Fig. 5A DR2). Oriented air-dried and ethylene-glycol-solvated mounts of the <2 μ m grain size fractions were scanned from 1 to 30 °2 θ with a step size of 0.05 °2 θ and a count time of 4 s per step (Fig. 5B DR2).

XRD tracings for experimentally sheared gouges reveal the formation of amorphous phases on the slip surface as result of frictional heating (Fig. 5a DR2). Among crystalline phases (Tab.4 DR2), quartz is the most abundant mineral with an average content of 44%, followed by albite (23%), phyllosilicates (18%), calcite (7%), k-feldspar (6%) and ankerite (2%). The <2 grain size fraction is mainly composed of non-clay minerals (quartz, plagioclase, k-feldspar, calcite) and of a clay mineral assemblages constituted by illite (68%), chlorite (18%), kaolinite (11%) and mixed layer I-S (2%; Fig. 5b DR2). Sand sheared at seismic slip rates (1 m/s) and normal stress of 14 MPa does not show the typical mixed layer I-S composition of natural samples (i.e, R0 I-S with an illite content of 30% in Tab. 3 DR2) but display long-range ordered (R3) I-S which are peculiar of black gouges (Fig. 5b DR2). This mineralogical occurrence is due to temperature increase during shear (frictional heating) and is similar to what observed in the studied fault zones. The lack of palygorskite, mixed layer C-S and pyrophyllite in the experimentally sheared gouges with respect to the natural samples is due to the limitation imposed by the experimental condition, where fluids cannot be circulated in the deforming rocks, failing to supply those nutrients which favour the chemical reactions and mineral transformations observed in the natural environmental conditions.

Item DR3. Temperature Calculations

The bulk temperature rise within a slip zone with thickness h can be calculated by (Carslaw and Jaeger, 1959; Rice, 2006):

$$\Delta T = \frac{\mu \sigma_n d}{\rho c_p h} \quad \text{Eq. 1}$$

when $h > 4\sqrt{\frac{\kappa d}{v}}$, i.e. in the adiabatic heating case, and by

$$\Delta T = \frac{\mu \sigma_n \sqrt{vd}}{\rho c_p \sqrt{\pi \kappa}} \quad \text{Eq. 2}$$

when $h \leq 4\sqrt{\frac{\kappa d}{v}}$, i.e. the slip zone is treated as a plane of zero thickness and heat diffusion is

accounted for; where μ is the friction coefficient, σ_n is the normal stress, d is the displacement, ρ is the rock density, c_p is the specific heat capacity and κ is the thermal diffusivity.

The temperature rise produced by earthquakes (magnitude up to M_w 5) that propagate along localised slip zones with the minimum thickness as the one observed in the field for the black gouge layers ($h = 5$ mm) has been calculated by using Eq. 1 (Fig. 6 DR3). The following physical properties and parameters, inferred for the black gouge decorated slip zones, have been used during our calculations: $d = 0.001$ (M_w 1) – 0.1 (M_w 5) m (Sibson, JSG 1983); $\mu = 0.7$ (see Table 5

DR4); $\sigma_n = 22$ MPa for dry conditions ($P_f = 0$) at about 1 km depth; effective normal stress $\sigma'_n = \sigma_n - P_f = 13.2 - 4.4$ MPa for hydrostatic ($\lambda=0.4$) and sub-lithostatic ($\lambda=0.8$) pore fluid pressure conditions, respectively have also been used (where λ is the pore fluid factor); $\rho = 2200$ kg/m³; $c_p = 752$ J/kgK was used as the specific heat capacity of quartz, the main mineralogical components in the host rocks (Clauser, and Huenges, 1995). We used the widely assumed average standard value of slip velocity=1 m/s (same as for the experiments).

The temperature rise produced during the laboratory experiments by sliding at sub-seismic and seismic slip rates has been calculated by using Eq. 1 and Eq. 2 depending on the microstructural evidence for slip localisation and the thickness of the deformed layer (Fig. 7 DR3). At sub-seismic

slip rates, the initial thickness of the gouge layer ($h \sim 2$ mm) satisfies the condition $h \leq 4\sqrt{\frac{\kappa d}{v}}$,

hence, Equation 2 (DR3) was used for temperature calculation. Microstructural observations from samples recovered after experiments at seismic slip rates, show the development of an irregular slip zone whose thickness is difficult to be defined. These observations and the initial thickness of

the gouge layer ($h \sim 2$ mm), which just satisfies the condition $h > 4\sqrt{\frac{\kappa d}{v}}$, justify the use of Equation

1 (DR3) for temperature calculation. Temperatures calculated by using Equation 2 (DR3) are also plotted on the diagram in Fig. 7 DR3, under the assumption of slip localization and, hence,

$h \leq 4\sqrt{\frac{\kappa d}{v}}$. Note that calculated temperatures have been added to a background temperature of

25 °C inferred at 1 km depth. The following physical properties were used for temperature calculations: $\rho = 2200$ kg/m³; $\kappa = 1.0 \cdot 10^{-6}$ m²s⁻¹ and $c_p = 752$ J/kgK was used as the specific heat capacity of quartz, the main mineralogical components in the host rocks (Clauser, C., Huenges, E., 1995. Thermal conductivity of Rocks and Minerals. In: Aherens J.T. (Ed.), Rock Physics and Phase Relations. A Handbook of Physical Constants. AGU Reference Shelf 3, pp. 105-126). The mechanical parameters d , μ , σ_n , v used for the temperature calculations are those reported in Table 5 DR4.

Item DR4. Experimental Apparatus, Sample Assembly and Mechanical Data

Low- to high-velocity rotary shear apparatus

Friction experiments (Table 5 DR4) were performed by using a low to high velocity rotary shear apparatus (Model MIS-233-1-77, Fig. 8 DR4) built by the Marui & Co., LTD Company (Osaka, Japan). The loading frame is very rigid, made of assembled steel plates and set up in a vertical configuration, secured to floor by a base plate (Fig. 8 DR4). The experiments were performed at room temperature and humidity conditions on fine-grained ($\phi \sim 230$ μ m) incohesive sands at slip rates $v = 100$ μ m/s - 1 m/s, normal stresses $\sigma_n = 7$ -14 MPa (Table 5 DR4). A synthetic fault zone was created by sandwiching 3 g of gouge between two stainless steel cylinders (25 mm in diameter), whose ends were machined with radial grooves of 500 μ m height, to simulate slip surface roughness (Fig. 9 DR4). The specimen assemblage was confined by a Teflon ring to limit gouge loss during the experiments (Fig. 9 DR4).

The upper, main shaft of the apparatus is driven by an electric, servo-controlled motor with 11kW power, 70 Nm rated torque and maximum rotation speed of 1500 rpm (Fig. 8 DR4). The electric servo motor can be either controlled in the manual or digital mode; the latter by a signal generator DF1906 (NF corporation), with a range of $\pm 10V$ and a resolution of $\pm 0.0002V$. Revolving speed of the main shaft ranges from 1.5 – 1500 rpm, when using the high speed mode (servo motor directly connected to the main shaft with a reduction gear ratio of 1:1). In the medium ($1.5 \cdot 10^{-3}$ – 1.5 rpm) and low speed mode ($1.5 \cdot 10^{-6}$ – $1.5 \cdot 10^{-3}$ rpm), the step down of the servo motor rotation speed is achieved by clutches and reduction gears in the gearbox (Fig. 8 DR4), with reduction gear ratios of 1:1000 and 1:1000000, respectively. The range of peripheral slip rates applicable to samples with outer diameter of 25mm is from about 6 cm/y to about 2 m/s. The apparatus can accelerate to the maximum peripheral target speed of 2 m/s in 205 – 270 ms at normal stresses $\sigma_n = 3$ and 18 MPa, respectively with acceleration of $3.7 - 4.9 \text{ m/s}^2$, respectively.

Axial load is applied to the lower main shaft by a pneumatic piston (Bellofram type cylinder) with 82 mm stroke, and able to produce a thrust of 10 kN (Fig. 8 DR4). The axial load system is equipped with a high precision air regulator to reduce and automatically correct the load fluctuation during loading. Axial load measurements are performed by a thin compression load cell (strain gauge type, Fig. 8 DR4), whose capacity is 10kN, and rated output of $2 \text{ mV/V} \pm 0.5\%$. Axial load cell resolution is $\pm 0.005 \text{ kN}$.

Torque values attained during the experiments are measured by two compression load cells (strain gauge type) (Fig. 8 DR4), that are activated by a torque bar fixed to the lower, main shaft. The load cell capacity is 1 kN, with a rated output of $2 \text{ mV/V} \pm 0.5\%$. Torque cell resolution is $\pm 5 \cdot 10^{-4} \text{ kN}$.

The axial displacement values attained during the experiments are measured by a high sensitivity displacement gauge (strain gauge type) with capacity of 10 mm and rated output of $5 \text{ mV/V} \pm 0.1\%$ (Fig. 8 DR4). Axial displacement resolution is $\pm 2 \cdot 10^{-3} \text{ mm}$.

The revolution speed and the cumulative number of revolutions are measured by a tachometer and a pulse counter, respectively; based on the pulses measured by a rotary encoder with capacity of 3600 pulses/revolution (Fig. 8 DR4).

Sample assembly and experimental determination of slip rate and slip for cylindrical samples.

We performed 14 experiments at room temperature and humidity conditions with a high to low velocity rotary shear friction apparatus (Fig. 9 DR4). Experiments were performed on fine-grained ($\phi \sim 230 \mu\text{m}$) incohesive sands made of quartz, plagioclase, K-feldspar, phyllosilicates (clay minerals, chlorite and mica) at slip rates ranging from $100 \mu\text{m/s}$ to 1 m/s , normal stresses $\sigma_n = 7\text{-}14 \text{ MPa}$ (Table 5 DR4). A synthetic fault zone was created by sandwiching 3 g of gouge between two stainless steel cylinders (25 mm in diameter), whose ends were machined with radial grooves of $500 \mu\text{m}$ height, to simulate slip surface roughness (Fig. 9 DR4). The specimen assemblage was confined by a Teflon ring to limit gouge loss during the experiments. Teflon rings were cut and tightened to the stainless cylinder by a hose clip; their inner edges being machined to reduce their sharpness (Fig. 9 DR4). The assembled stainless steel cylinders + gouge material are mounted on

the sample holders where they are kept fixed to the main shafts and axially aligned during the experiments by a hydraulic mechanical lock.

Given the cylindrical shape of the stainless steel cylinders, sandwiching the sand gouges, the determination of slip rate v in the gouge is problematic, since v increases with sample radius r ($v = \omega r$; ω is the rotary speed). During the experiments, the revolution rate of the motor R and the torque T are measured. It follows that the slip rate for the gouge is obtained in terms of "equivalent slip rate" V_e (see for details Shimamoto and Tsutsumi, *Struct. Geol.* 39, 65-78, 1994; Hirose & Shimamoto, *J. Geophys. Res.* 110, doi:10.1029/2004JB003207, 2005) by

$$V_e = \frac{4 \pi R r}{3} \quad \text{Eq. 1.}$$

We refer the equivalent slip rate simply as slip rate v in the paper and, as a consequence, the slip d is

$$d = V_e t \quad \text{Eq. 2.}$$

where t is the time.

References

- Balsamo, F. & Storti, F., 2011. Size-dependent comminution, tectonic mixing, and sealing behavior of a "structurally oversimplified" fault zone in poorly lithified sands: Evidence for a coseismic rupture? *Geological Society of America Bulletin* 123, 601-619 (2011).
- Balsamo, F., Bezerra, F.H., Vieira, M., and Storti, F., 2013, Structural control on the formation of iron oxide concretions and Liesegang bands in faulted, poorly lithified Cenozoic sandstones of the Paraíba basin, Brazil: *Geological Society of America Bulletin*, v. 125, p. 913–931, doi:10.1130/B30686.1.
- Carlsaw and Jaeger, 1959. *Conduction of Heat in Solids*, 2nd edition.
- Clauser, C., Huenges, E., 1995. Thermal conductivity of Rocks and Minerals. In: Aherens J.T. (Ed.), *Rock Physics and Phase Relations. A Handbook of Physical Constants*. AGU Reference Shelf 3, pp. 105-126).
- Jagodzinski, H. Eindimensionale Fehlordnung in Kristallen und ihr Einfluss auf die Röntgen Interferenzen. *Acta Crystallogr.* 2, 201–207 (1949).
- Leon y Leon, C.A., 1998. New perspectives in mercury porosimetry. *Advances in Colloid and Interface Science*, 76–77, pp. 341–372.
- Moore, D. M. & Reynolds, R. C., Jr. *X-Ray diffraction and the identification and analysis of clay minerals* 1-378 (Oxford University Press, 1997)
- Rice, J. R., 2006. Heating and weakening of faults during earthquake slip. *Journal of Geophysical Research -Solid Earth* 111.

- Storti, F., and Balsamo, F., 2010, Particle size distributions by laser diffraction: Sensitivity of granular matter strength to analytical operating procedures: *Solid Earth*, v. 1, p. 25–48, doi:10.5194/se-1-25-2010.
- Storti, F., Balsamo, F., and Salvini, F., 2007, Particle shape evolution in natural carbonate granular wear material: *Terra Nova*, v. 19, p. 344–352, doi:10.1111/j.1365-3121.2007.00758.x.
- Washburn, E.W., 1921. Note on a method of determining the distribution of pore sizes in a porous material. *Proceedings of the National Academy of Sciences USA*, 7, pp. 115–116.

Table DR1. Grain size statistical parameters of undeformed and faulted sediments

Sample Name	Structural domain	Span	Mean diameter (μm)	% SAND	% SILT	% CLAY
FAULT 1						
Fault 1- RN 9.1 ^(*)	UND HW	1.44	236.74	94.30	5.49	0.21
Fault 1- RN 9.2	HW DZ (zone of DB)	2.10	147.38	73.43	23.13	3.43
Fault 1- RN 9.3a	HW DZ (space between DB)	2.73	204.54	76.08	21.11	2.81
Fault 1- RN 9.3b	HW DZ (shear band)	3.92	110.37	51.88	39.56	8.56
Fault 1- RN 9.4	FC (Black Gouge)	7.97	132.96	45.98	42.22	11.81
Fault 1- RN 9.5 ^(P)	FC (Foliated cataclasite)	8.74	142.42	46.50	40.92	12.58
Fault 1- RN 9.6	FW DZ (zone of DB)	2.66	164.68	68.62	26.57	4.81
Fault 1- RN 9.7	FW DZ (zone of DB)	4.96	321.55	70.90	24.39	4.71
Fault 1- RN 9.8	FW DZ (shear band)	4.35	119.68	52.27	39.81	7.92
Fault 1- RN 9.9	FW DZ (zone of DB)	3.01	147.41	64.19	30.45	5.36
Fault 1- RN 9.10	FW DZ (zone of DB)	4.35	321.90	71.35	23.52	5.13
Fault 1- RN 9.11	FW DZ (DB)	5.98	216.61	59.80	33.35	6.85
Fault 1- RN 9.12	FW DZ (DB)	3.08	440.94	82.63	14.81	2.56
Fault 1- RN 9.13	UND FW	2.24	584.92	90.04	8.94	1.03
Fault 1- RN 9.14	FW DZ (DB)	4.76	336.13	70.78	24.40	4.82
FAULT 2						
Fault 2- RN 29C	UND HW	1.55	218.54	91.47	8.17	0.36
Fault 2- RN 29D	UND HW	1.47	256.35	93.11	6.67	0.22
Fault 2- RN 29B	HW DZ (zone of DB)	2.55	113.66	60.95	34.09	4.96
Fault 2- RN 29E	FC (Foliated cataclasite)	3.39	128.01	58.40	35.68	5.93
Fault 2- RN 29A ^(P)	FC (Black Gouge)	10.67	80.97	33.68	46.24	20.08
Fault 2- RN 29A2	FC (Black Gouge)	4.37	86.52	46.48	43.62	9.90
Fault 2- RN 29G	FC (Foliated cataclasite)	3.54	221.50	66.21	28.34	5.45
Fault 2- RN 29F	UND FW	1.59	368.08	93.98	5.82	0.20
FAULT 3						
Fault 3- RN 32D	UND HW	3.58	435.32	77.74	19.18	3.08
Fault 3- RN 32C	FC (Foliated cataclasite)	6.54	300.61	62.85	30.71	6.44
Fault 3- RN 32B	FC (Foliated cataclasite)	4.83	78.63	42.34	48.99	8.67
Fault 3- RN 32F ^(P)	FC (Black Gouge)	7.22	80.65	38.70	40.98	20.32
Fault 3- RN32A	FC (Black Gouge)	6.21	78.17	36.40	44.37	19.23
Fault 3- RN 32E	FC (Foliated cataclasite)	3.43	148.62	63.46	32.74	3.80
Fault 3- RN 32G ^(P)	FC (Foliated cataclasite)	2.94	116.97	57.97	34.37	7.66
Fault 3- RN 32H	FC (Foliated cataclasite)	3.79	99.07	51.04	40.53	8.43
Fault 3 - RN 30B ^(P)	UND FW	2.07	639.73	93.38	6.14	0.49

(UND=undeformed sand; HW=hanging wall; FW=footwall; DZ=damage zone; FC=fault core; DB=deformation band; ^(*)=sand used for friction experiment; ^(P)=porosity analysis). Displacement Fault 1= 21.3 m; Displacement Fault 2= 13.6 m; Displacement fault 3=41.7 m.

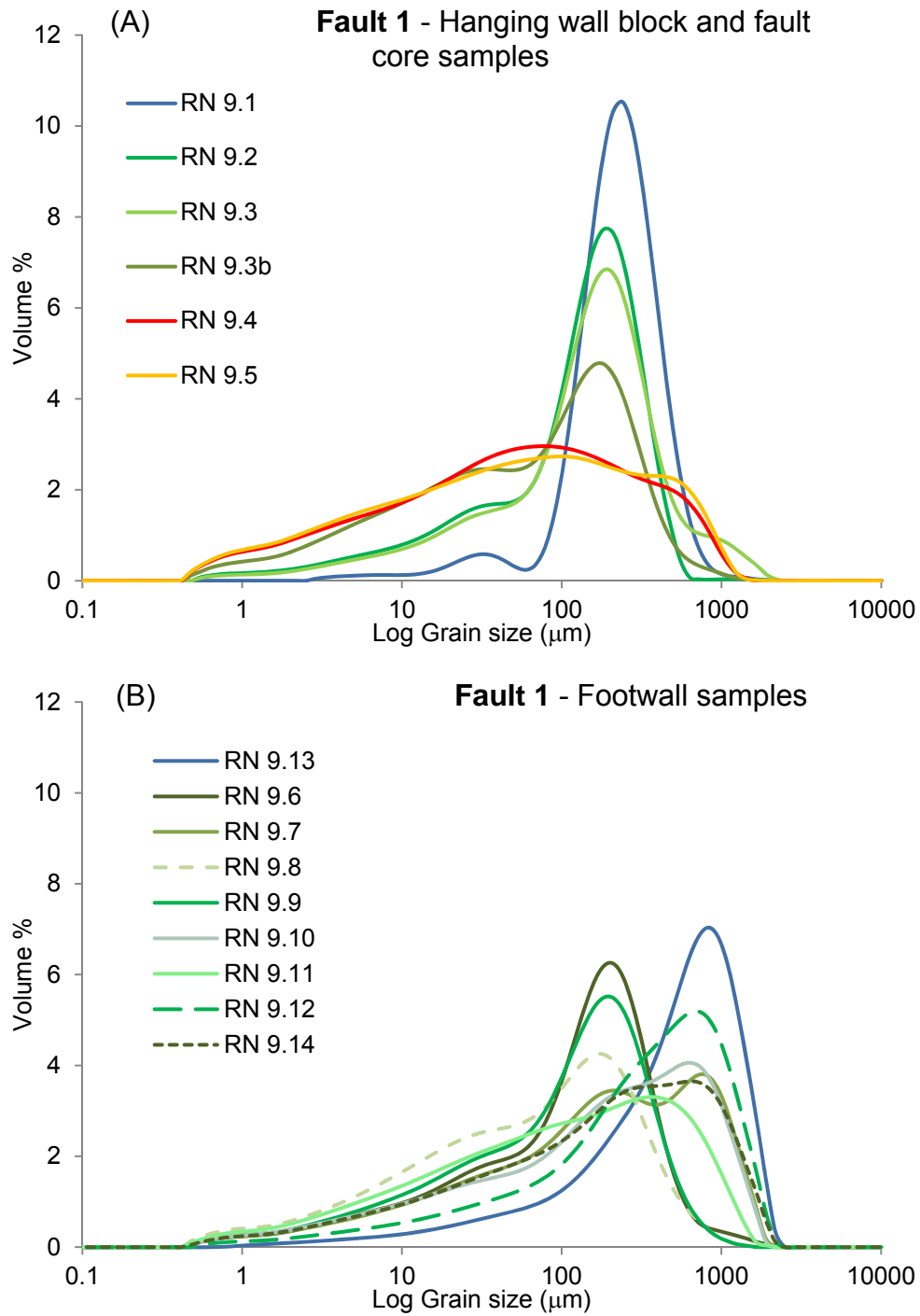


Figure DR1. Grain size distribution curves in the Fault 1. (A) Undeformed (blue), damage zone (green) and fault core (cataclasite in orange and black gouge in red) samples in the hanging wall block. (B) Undeformed and damage zone samples in the footwall block.

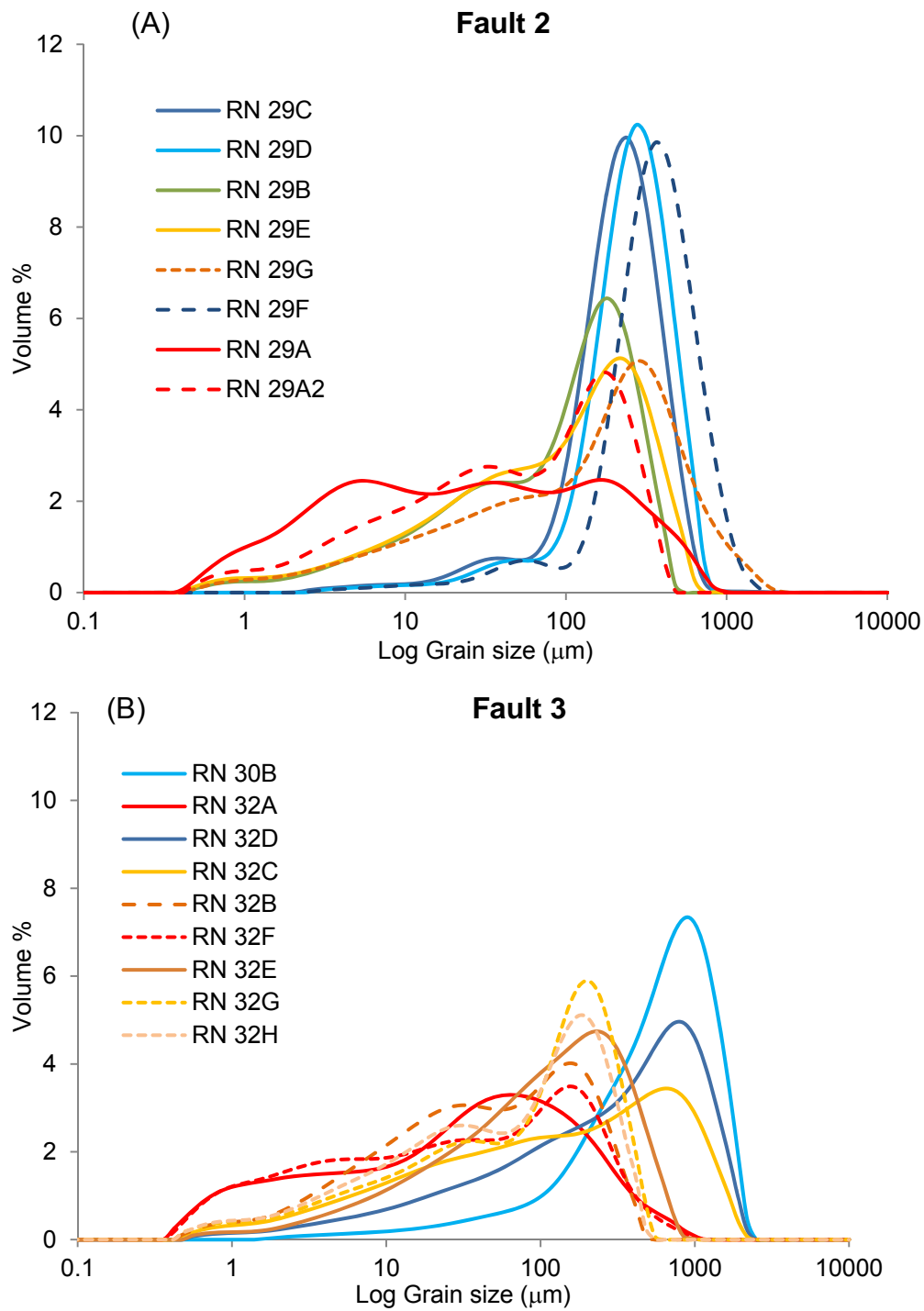


Figure DR2. Grain size distribution curves in Fault 2 (A) and Fault 3 (B). Undeformed samples are in blue, damage zone samples in green, foliated cataclasites in fault core in orange, and black gouges in red.

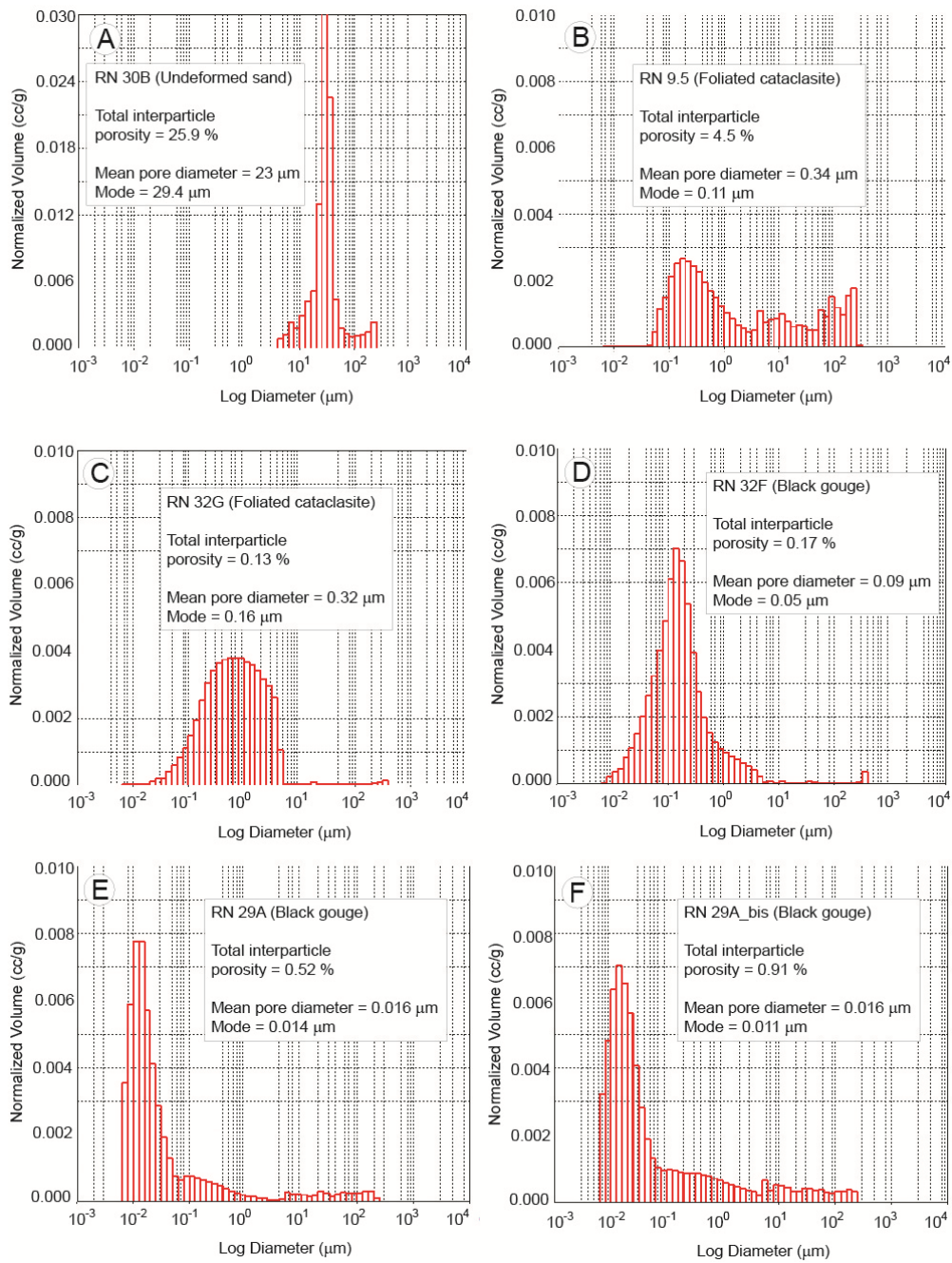


Figure DR3. Pore size distributions and statistical results of an undeformed sand (A), foliated cataclasites within the fault core (B, C) and black gouges localized within the foliated cataclasites (D-F). Vertical axes indicate the normalized volume of injected mercury (cc/g), horizontal axes indicate the diameter of pore size (μm).

Table DR2. X-ray semi-quantitative analysis of whole-rock composition of natural samples.

Fault/sample	Structural domain	whole-rock composition						
		Qtz	Cal	Kfs	Ab	Phy	Ank	Dol
Fault 1 -RN 2	Host sediments	38	3	6	32	19	2	0
Fault 1 - RN 6	Host sediments	40	6	5	32	14	2	0
Fault 1 - RN 4 DB	Damage zone	32	6	8	38	14	2	0
Fault 1 - RN 9 DB	FW Damage zone	36	1	7	30	24	2	0
Fault 1 - RN 9 DB	Damage zone	43	2	7	33	14	2	0
Fault 1 -RN 9 DB	HW Damage zone	42	8	7	28	13	2	0
Fault 1 - RN 2 FC	Foliated cataclasite	34	1	7	38	18	2	0
Fault 1 - RN 4 FC	Foliated cataclasite	27	7	11	33	20	2	0
Fault 1 - RN 6 FC	Foliated cataclasite	29	7	5	37	21	2	0
Fault 1 - RN 7 FC	Foliated cataclasite	37	10	6	28	17	2	0
Fault 2 - RN 29a FC	Foliated cataclasite	36	2	8	34	18	2	0
Fault 3 - RN 32 FC	Foliated cataclasite	44	5	6	32	8	3	0
Fault 1 - RN 9 FC	Foliated cataclasite	41	5	6	27	19	2	0
Fault 1 - RN 9g	foliated cataclasite	26	3	5	16	49	1	0
Fault 3 - RN 32g	Black gouge	41	6	6	24	18	2	1
Fault 3 - RN 32a	Black gouge	34	1	5	35	23	2	0

Qtz: quartz, Cal: calcite, Kfs: K-feldspar, Ab: albite, Phy: phyllosilicate minerals, Ank: ankerite, Dol: dolomite. (DB: deformation bands, FC: fault core, FW: footwall, HW: hanging wall).

Table DR3. X-ray semi-quantitative analysis of the <2µm grain-size fraction of natural samples.

Sample	Structural domain	X-ray quantitative analysis of the <2µm grain-size fraction (% wt.)								R	%I in I-S	%C in C-S
		Prl	Plg	I	I-S	C-S	Kln	Chl	Other			
RN 2	Host sediments	0	0	59	5	0	18	18	Qtz+Ab+Kfs	0	30	
RN 6	Host sediments	0	0	53	15	0	17	15	Qtz+Cal+Ab+Kfs	0	30	
RN 4dz	Damage zone	0	0	61	6	0	16	17	Qtz+Cal+Ab+Kfs	0	30	
RN 9 fw db	Damage zone	0	0	78	3	0	9	10	Qtz+Ab+Kfs	0	30	
RN 9 db	Damage zone	0	9	72	3	0	8	8	Qtz+Ab+Kfs	0	30	
RN 9 hw db	Damage zone	0	0	72	4	0	8	16	Qtz+Cal+Ab+Kfs	0	30	
RN 2 FC	Foliated cataclasite	0	0	66	1	0	16	17	Qtz+Ab+Kfs	0	30	
RN 4 FC	Foliated cataclasite	0	0	65	3	0	16	16	Qtz+Cal+Ab+Kfs	0	30	
RN 6 FC	Foliated cataclasite	0	0	67	3	0	16	14	Qtz+Cal+Ab+Kfs	0	30	
RN 7 FC	Foliated cataclasite	0	0	61	4	0	17	18	Qtz+Cal+Ab+Kfs	0	35	
RN 29 a FC	Foliated cataclasite	0	0	78	0	19	2	1	Qtz+Ab+Kfs	-	-	80
RN 32 FC	Foliated cataclasite	0	0	74	2	0	11	13	Qtz+Gy+Ab+Kfs	0	35	
RN 9 FC	Foliated cataclasite	0	24	49	3	9	6	9	Qtz+Cal+Ab+Kfs	1	75	80
RN 9 g	Foliated cataclasite	0	51	33	1	7	3	5	Qtz+Cal+Ab+Kfs	1	75	80
RN 32 g	Black gouge	tr	0	70	1	0	11	18	Qtz+Ab+Kfs	3	90	
RN 32 a	Black gouge	4	0	61	6	0	14	15	Qtz+Ab+Kfs	3	90	

Prl: pyrophyllite, Plg: palygorskite, I: illite, I-S: mixed layer illite-smectite, C-S: mixed layer chlorite-smectite, Kln: kaolinite, Chl: chlorite, Qtz: quartz, Cal: calcite, Kfs: K-feldspar, Ab: albite, Gy: gypsum, R: stacking order (Jagodzinski, 1949), %I in I-S: illite content in mixed layer illite-smectite, %C in C-S: chlorite content in mixed layer C-S. tr stands for traces (<1% wt.).

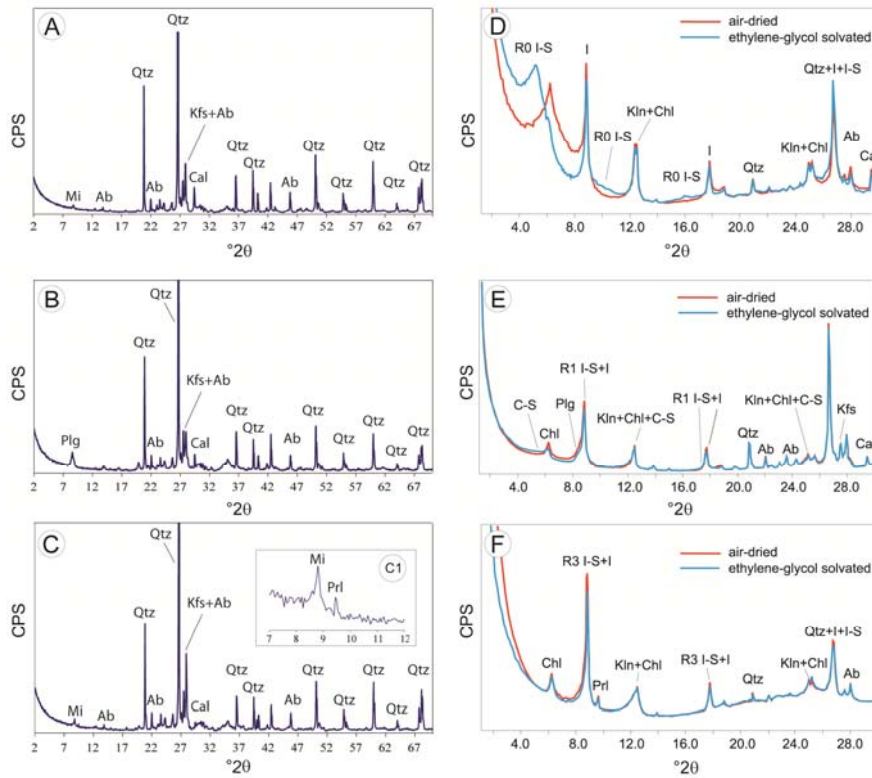


Figure DR4. Selected X-ray patterns of natural whole-rock samples (A, B and C) and <2μm grain-size fraction (D, E and F). A and D refer to host sediment, B and E to foliated cataclasite and C and F to black gouge. Note the presence of pyrophyllite in the black gouge (C1). Acronyms - Qtz: quartz, Cal: calcite, Kfs: K-feldspar, Ab: albite, Mi: Mica; Plg: palygorskite; Prl: pyrophyllite; I: illite, I-S: mixed layer illite-smectite, Kln: kaolinite; Chl: chlorite

Table DR4. Whole-rock composition of sand sheared at seismic slip rate of 1 m/s and normal stress of 14 MPa (Du_192 and Du_207) and 7 MPa (Du_191 and Du_206).

Sample	whole-rock composition						
	Qtz	Cal	Kfs	Ab	Phy	Ank	Am
Du_192	43	5	5	21	22	2	2
Du_207	44	6	6	23	18	2	1
Du_191	43	9	6	23	15	2	2
Du_206	40	9	7	23	17	2	2

Qtz: quartz, Cal: calcite, Kfs: K-feldspar, Ab: albite, Phy: phyllosilicates, Ank: ankerite; Am: amorphous phases.

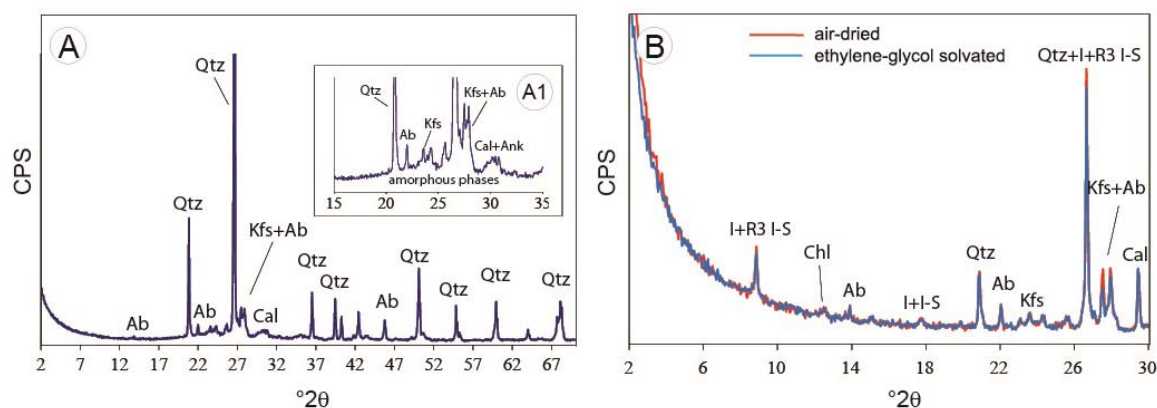


Figure DR5. Selected X-ray patterns of whole-rock sample (A) and <2 μ m grain-size fraction (B) for host sediments sheared at slip rate of 1 m/s and normal stress (σ_n) of 14 MPa. Note the low signal-to-noise ratio in the 15-30 $^\circ 2\theta$ interval due to the formation of amorphous material.

Acronyms - Qtz: quartz, Cal: calcite, Kfs: K-feldspar, Ab: albite, Ank: ankerite, I: illite, I-S: mixed layer illite-smectite, Chl: chlorite

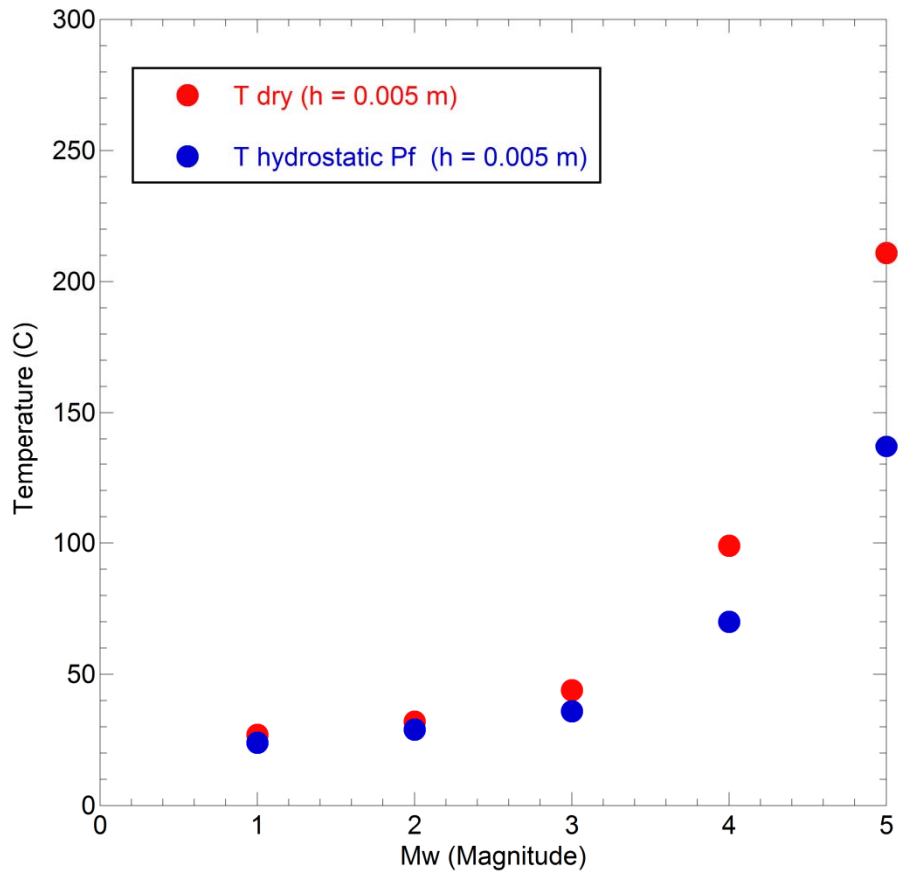


Figure DR6. Temperature vs. earthquakes magnitude M_w calculated for localised slip zones observed in the field for the black gouge layers with thickness ($h = 5$ mm) (See DR3 for details). Note that temperatures calculated by Eq. 1 (DR3) have been added to a background temperature of 25 °C inferred at 1 km depth.

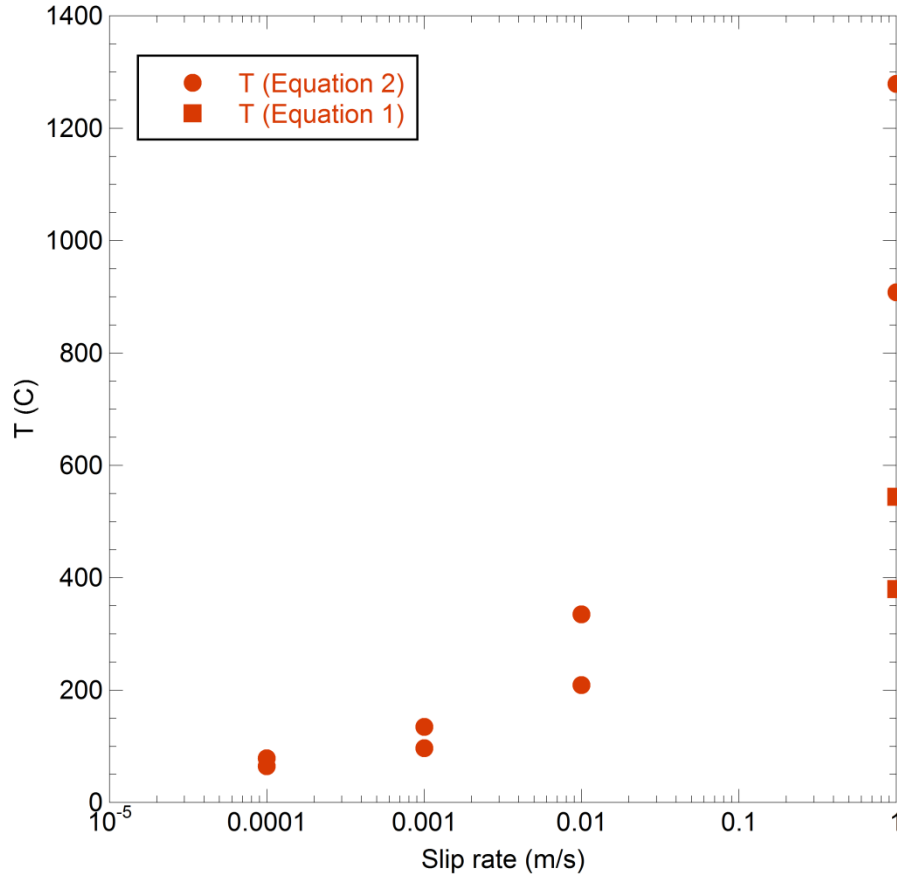


Figure DR7. Temperature vs. slip rate calculated for experiments performed at sub-seismic ($v \leq 0.01$ m/s) and seismic (1 m/s) slip rates. At sub-seismic slip rates, the initial thickness of the gouge

layer ($h \sim 2$ mm) satisfies the condition $h \leq 4\sqrt{\frac{\kappa d}{v}}$, hence, Equation 2 (DR3) was used for

temperature calculation. Microstructural observations from samples recovered after experiments at seismic slip rates, show the development of an irregular slip zone whose thickness is difficult to be defined. These observations and the initial thickness of the gouge layer ($h \sim 2$ mm), which just

satisfies the condition $h > 4\sqrt{\frac{\kappa d}{v}}$, justify the use of Equation 1 (DR3) for temperature calculation.

Temperatures calculated by using Equation 2 (DR3) are also plotted on the diagram, under the

assumption of slip localization and, hence, $h \leq 4\sqrt{\frac{\kappa d}{v}}$. Note that calculated temperatures have

been added to a background temperature of 25 °C inferred at 1 km depth.

Table DR5.

<i>Test #</i>	σ_n [MPa]	v [m/s]	μ_i	μ_p	μ_f	d [m]	d_{iw} [m]
Du_210	7	10^{-4}	0.59	0.69	0.69	1.24	-
Du_211	14	10^{-4}	0.65	0.73	0.67	1.22	0.67
Du_187	7	10^{-3}	0.68	0.69	0.62	1.5	1.14
Du_188	14	10^{-3}	0.63	0.66	0.64	1.15	0.80
Du_200	7	10^{-2}	0.67	0.73	0.73	1.23	-
Du_201	14	10^{-2}	0.65	0.70	0.64	1.29	0.61
Du_198	14	10^{-1}	0.62	0.73	0.73	1.24	-
Du_213	7	$5 \cdot 10^{-1}$	0.69	0.72	0.57	1.1	0.82
Du_215	14	$5 \cdot 10^{-1}$	0.67	0.73	0.48	0.8	0.41
Du_191	7	1	0.63	0.73	0.39	1.28	0.88
Du_206	7	1	0.67	0.74	0.32	1.29	0.39
Du_192	14	1	0.69	0.72	0.47	1.3	0.34
Du_207	14	1	0.67	0.74	0.38	0.8	0.20
Du_208	14	1	0.66	0.74	0.46	0.66	0.24

σ_n : Normal stress; v : Slip rate; μ_i : Friction coefficient values attained at the beginning of the experiment, soon after the attainment of the target slip rate; μ_p : Friction coefficient values attained at the end of any phase of slip-hardening shown during the experiments; μ_f : Friction coefficient values attained at the end of the experiment before slip arrests; d : Displacement; d_{iw} : Displacement attained at the beginning of any phase of slip-weakening observed during the experiments.

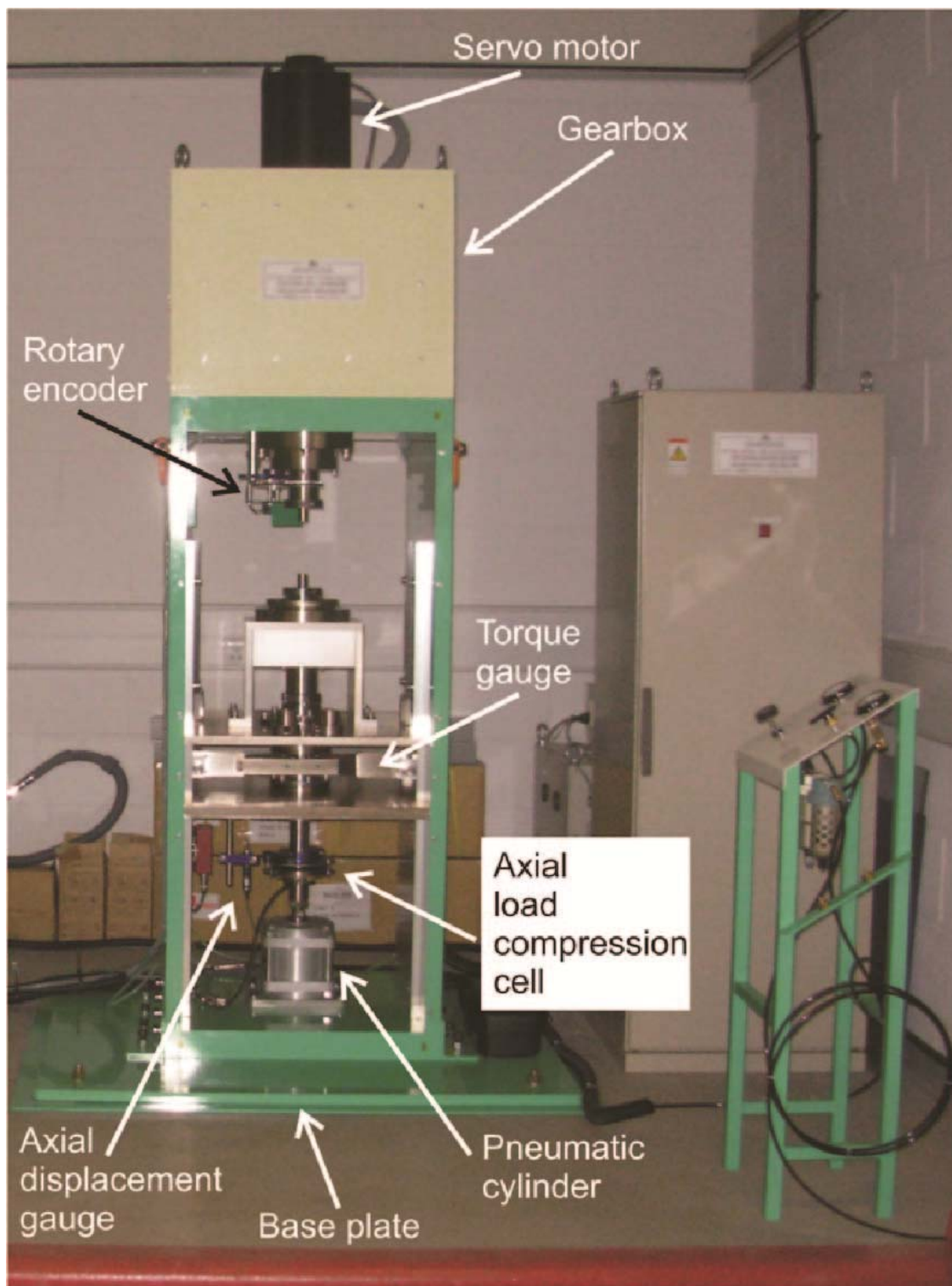


Figure DR8. Low- to high-velocity rotary shear apparatus installed in the Rock Mechanics Laboratory at Durham University (UK).

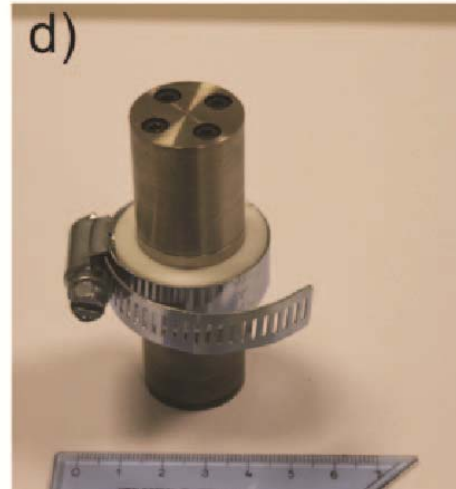
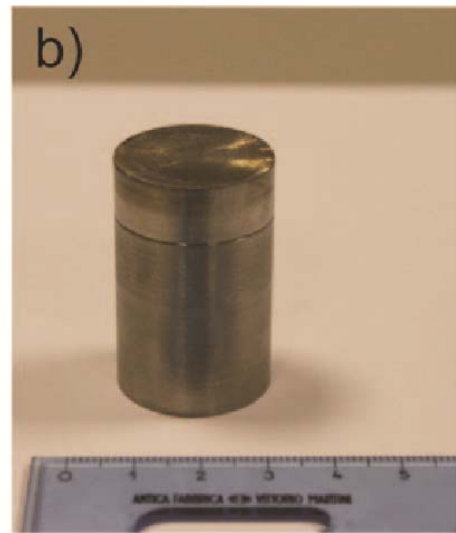


Figure DR9. (a) Disassembled components of the sample assembly used during the experiments; (b) Assembled stainless steel cylinders. (c) A Teflon ring is cut and then tightened to the stainless steel cylinders by a hose clip to confine gouges during the experiments. (d) Sample assembly in its fully assembled configuration.